Spin wave dispersion in perpendicularly magnetized synthetic antiferromagnets

Tengfei Zhang,[1,*] Chaozhong Li,[1,*] Qian Zhao,[1] Zimu Li,[1] Quwen Wang,[1] Guoqiang Yu,[2,3] Xiufeng Han,[2,3] Guozhi Chai,[1] Senfu Zhang,[1] Qingfang Liu,[1] Jianbo Wang,[1,4] and Jinwu Wei[1,†]

[1]*Key Laboratory for Magnetism and Magnetic Materials of the Ministry of Education, Lanzhou University, Lanzhou 730000, China*
[2]*Beijing National Laboratory for Condensed Matter Physics, Institute of Physics, Chinese Academy of Sciences, Beijing 100190, China*
[3]*Center of Materials Science and Optoelectronics Engineering, University of Chinese Academy of Sciences, Beijing 100049, China*
[4]*Key Laboratory of Special Functional Materials and Structural Design, Ministry of Education, Lanzhou University, Lanzhou 730000, China*

(Received 8 October 2023; revised 15 December 2023; accepted 19 January 2024; published 5 February 2024)

The spin wave is a promising candidate medium to be used as an information carrier and for processing. Knowledge of the spin wave dispersion relation is a prerequisite for its application and the design of devices. Here, we report on spin wave dispersion in perpendicularly magnetized synthetic antiferromagnets (p-SAFs), consisting of two CoFeB layers and a thin W spacer layer. The Brillouin light scattering technique is employed to measure the spin wave dispersion relations as a function of the in-plane magnetic field and wave vector. Two resonance modes are observed in the finite range of the magnetic field, in which the configuration of the magnetic moments in two CoFeB layers can be divided into antiferromagnetic and ferromagnetic states. In addition, we observe a T-type region, where the magnetization in one CoFeB layer lies in the direction of the in-plane magnetic field and the other stays in the out-of-plane direction. The dependences of the frequency on the wave vector demonstrate the spin wave propagation in this case is reciprocal. We also theoretically derive the spin wave dispersion relation for p-SAFs based on the Landau-Lifshitz equation, which agree well with the experimental results.

DOI: 10.1103/PhysRevB.109.054406

I. INTRODUCTION

Spin waves are collective excitations of magnetic moments which carry spin angular momentum and can be used as information carriers. The quanta of spin waves are referred to as magnons, and the research field that utilizes spin waves for information transport and processing is known as magnonics [1–5]. Compared with the traditional information carrier, like conduction electrons, spin-wave-based information processing can significantly reduce Joule heating and operates in the frequency range from serval gigahertz to hundreds of terahertz. This attracts more attention due to its promising prospect in energy-efficient and ultrafast devices [6–8]. So far, most spin wave studies have mainly focused on ferromagnets (FMs) and ferrimagnets, including yttrium iron garnet [9–12] and permalloy films [13–15]. Recently, antiferromagnetic (AFM) spin waves have been stimulating interest due to several advantages. AFMs have greater thermal stability and the absence of stray magnetic fields [16]. Unlike FM spin wave devices using the amplitude and phase, AFM spin waves have not only right- and left-handed circular polarizations in an easy-axis AFM but also a linearly polarized mode in an easy-plane AFM, which have been observed in crystal AFMs such as MnF_2 [17], FeI_2 [18], and α-Fe_2O_3 [19], although some AFMs have gigahertz resonance frequencies due to the low magnetic anisotropy or weak exchange coupling, such as the canted α-Fe_2O_3 [20] and the layered AFM insulator $CrCl_3$ [21]. However, it is difficult to excite and manipulate spin waves in most AFMs because they have a high intrinsic frequency (up to the terahertz range) due to strong magnetic anisotropy and exchange coupling, which requires terahertz techniques to probe and strong magnetic field up to several Tesla [22–24]. Synthetic antiferromagnets (SAFs), formed through the weak interlayer exchange coupling between two FMs mediated by a sandwiched metallic layer, show the resonance frequency within the range of conventional microwave electronics (several tens of gigahertz) [25,26]. This facilitates the detection and manipulation of AFM spin waves.

Recent works have reported the spin wave in SAFs with easy-plane anisotropy or perpendicular magnetic anisotropy (PMA), which mainly focus on the spin wave nonreciprocity and resonance modes [27–29]. During the experiments, an external magnetic field was usually applied along the direction of Néel vector, as shown in Fig. 1(a). As the magnetic field increases, the magnetization states are divided into three regions: AFM state, spin-flop transition, and FM state [30]. Because of the interlayer coupling in SAFs, two resonance modes are observed, including acoustic mode (AM) and optic mode (OM), which represent the in-phase and out-of-phase precession, respectively [31]. For the situation that magnetic field is perpendicular to the Néel vector, however, it is rarely reported. In this paper, we experimentally study the spin wave dispersion in perpendicularly magnetized SAFs (p-SAFs) when an external magnetic field is perpendicular to the Néel vector, as shown in Fig. 1(b), in which the AM and OM are also observed in AFM and FM regions. Moreover,

*These authors contributed equally to this work.
†weijw@lzu.edu.cn

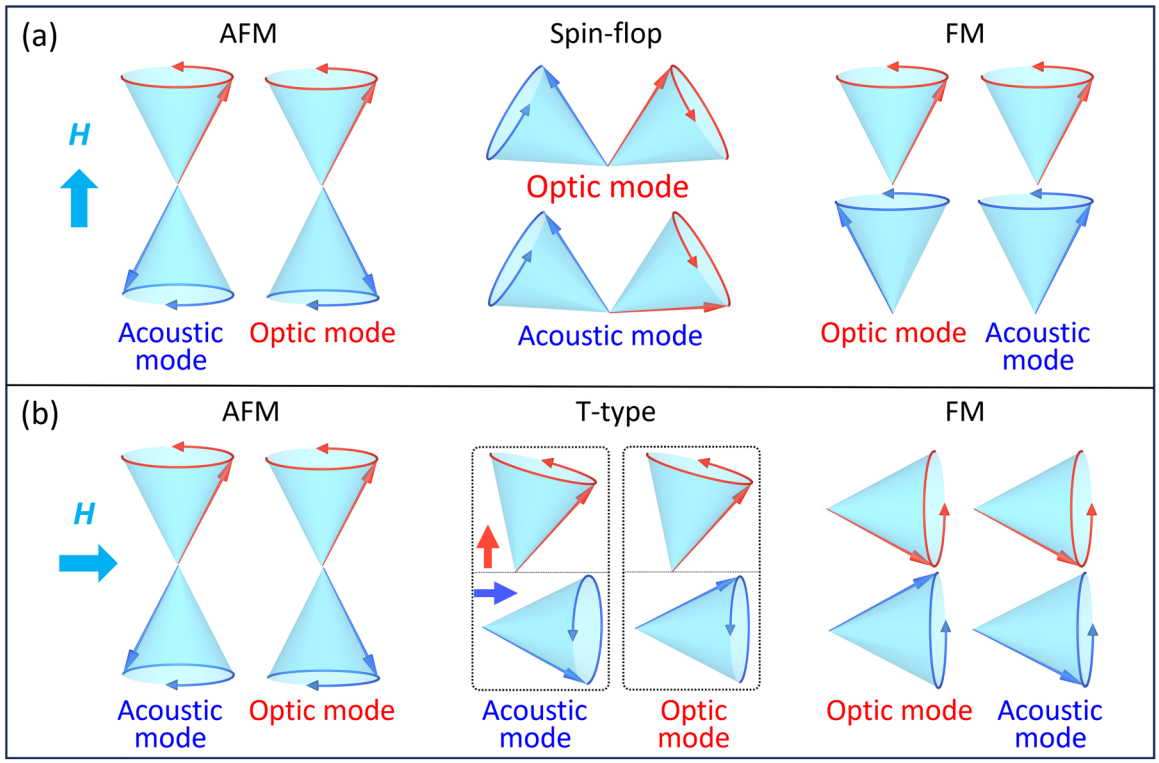

FIG. 1. Schematic diagram of resonance modes in perpendicularly magnetized synthetic antiferromagnets (p-SAFs). (a) The case of external magnetic field applied along the direction of the Néel vector. The magnetic moments in two ferromagnetic (FM) layers experience three states: antiferromagnetic (AFM), spin-flop transition, and FM state. The acoustic mode (AM) and optic mode (OM) are present in each magnetization state. (b) The case of magnetic field applied along the perpendicular direction of the Néel vector. The presentation of AM and OM in three different magnetization states: AFM, T-type, and FM state.

in the transition region between AFM and FM states, the magnetization state forms an upside-down T-type configuration, namely, two FM layers in p-SAFs have in-plane and out-of-plane magnetization, respectively. A theoretical model is proposed to explain the dispersion relations, which can fit well with the experimental results. This paper can facilitate the application of p-SAFs in spin-wave-based logic devices.

II. THEORETICAL MODEL

To understand the origin of spin wave dispersion in p-SAFs, we firstly model the magnetic dynamics by performing a macrospin simulation based on the Landau-Lifshitz (LL) equation. As shown in Fig. 2, the system consists of two FM layers with the same magnetization M_s and different PMAs (K_1 and K_2) and thicknesses (t_1 and t_2), in which the interlayer

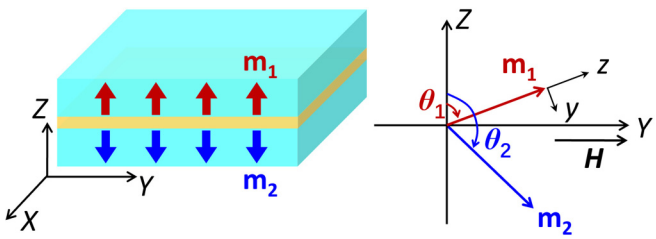

FIG. 2. Structure schematic of perpendicularly magnetized synthetic antiferromagnet (p-SAF), and a *XYZ* coordinate is established.

exchange energy per unit area is J_{ex}. The spin wave propagation is assumed to be along the X axis with wave vector k. The external magnetic field lies in the Y axis. The total energy density E per unit area can be given by

$$E = -\sum_{i=1,2} \mu_0 M_s t_i H_{ext} \cos\langle \vec{m}_i, \vec{H}_{ext} \rangle - \sum_{i=1,2} \left(t_i K_i - \frac{\mu_0 M_s^2 t_i}{2} \right) \times m_{Zi}^2 + J_{ex} \vec{m}_1 \cdot \vec{m}_2 + E_{DMI}, \quad (1)$$

where the first term is Zeeman energy, the second term is the demagnetization energy, the third term is interlayer exchange energy, and the last term is the interfacial Dzyaloshinskii-Moriya interaction (DMI) energy. Here, $\vec{m}_i$ is the magnetization of FM layer $i(=1, 2)$, and J_{ex} is a positive value for the AFM coupling. Based on the minimum of free energy, the equilibrium state of magnetization in a p-SAF is determined on the condition of various magnetic fields. Two sets of coupled LL equations in p-SAFs are thus established at the equilibrium state (see Appendix A for more detail). The effective field $\vec{H}_i$ acting on the magnetization $\vec{m}_i$ is thus given by $\vec{H}_i = -\nabla_{\vec{m}_i}(\frac{E}{\mu_0 M_s t_i}) + \vec{h}_{dip,i}$ [29]. Here, $\vec{h}_{dip,i}$ represents the dynamic dipolar field generated by the nonuniform distribution of the magnetic moments of spin waves, which can be obtained through Maxwell's relations. The detailed expressions of effective fields and dynamical dipolar fields can be seen in Appendix B.

To simplify the solution procedure, we introduce a new xyz coordinate, where the z axis is parallel to the magnetization at the equilibrium state and the x axis is parallel to the X axis, as shown in Fig. 2. The effective fields can be transformed from the XYZ coordinate to the xyz coordinate by using a rotation matrix. In the xyz coordinate, the magnetization and effective field in FM layer i can be expressed as

$$\vec{m}_i(x,t) = \begin{pmatrix} m_{xi}\exp[i(kx+\omega t)] \\ m_{yi}\exp[i(kx+\omega t)] \\ 1 \end{pmatrix}, \tag{2}$$

$$\vec{H}_{\text{eff},i} = \begin{pmatrix} H^x_{\text{eff},i} + h^x_{\text{dip},i} \\ H^y_{\text{eff},i} + h^y_{\text{dip},i} \\ H^z_{\text{eff},i} + h^z_{\text{dip},i} \end{pmatrix}, \tag{3}$$

where the effective fields consist of static and dynamic components. In the linear regime, the dynamic part of the effective field is proportional to $\vec{m}_i(x,t)$, which depends on the wave factor k. Considering a small oscillation of the magnetization around the equilibrium state, the LL equations $d\vec{m}_i/dt = -\gamma\vec{m}_i \times \vec{H}_{\text{eff},i}$ can be linearized as

$$\left(\frac{i\omega}{\gamma} + \hat{H}\right)\begin{pmatrix} m_{x1} \\ m_{y1} \\ m_{x2} \\ m_{y2} \end{pmatrix} = 0, \tag{4}$$

where γ is the gyromagnetic ratio and $\hat{H}$ is a fourth-order matrix. The resonance frequencies $f = \omega/(2\pi)$ can be thus obtained by solving the eigenvalues of coefficient matrix. The detailed elements of the fourth-order matrix are explicitly given in Appendix B. For the sake of simplicity, the eigensolutions of Eq. (4) can be obtained through the numerical method, which are used to explain the following experimental results.

III. SAMPLES AND EXPERIMENTS

To study the spin wave modes in p-SAFs, we fabricated $Co_{20}Fe_{60}B_{20}$ (CoFeB)/W/CoFeB multilayers. The sample structure is Si/SiO_x//W (1)/MgO (2)/CoFeB (t)/W (1)/CoFeB (0.9)/MgO (2)/W (2), where // means the Si/SiO_x substrate and the numbers in parentheses are thicknesses in nanometers. According to the difference of the dead layer of CoFeB films grown on the W and MgO layers, we prepared the uncompensated and nearly compensated SAFs, corresponding to the bottom thicknesses $t = 1.3$ and 1.6 nm, which are named p-SAF1 and p-SAF2, respectively. The two FM layers form AFM coupling through Ruderman-Kittel-Kasuya-Yoshida (RKKY) interaction using an ultrathin W spacer. The top W layer is used as a capping layer to protect the magnetic layers from oxidation. All samples were prepared by using a magnetron sputtering system with a 5×10^{-6} Pa base pressure. Subsequent annealing was performed at the temperature of 325 °C for 30 min in a vacuum furnace to induce strong PMA and interlayer exchange coupling. The excitation and detection of spin wave modes and propagation in p-SAFs were studied by employing wave-vector-resolved Brillouin light scattering (BLS). The hysteresis loops were measured by using a vibrating sample magnetometer (Lake Shore 8604). All measurements were performed at room temperature.

IV. RESULTS AND DISCUSSION

A. Static magnetic properties

Normalized magnetic hysteresis loops of p-SAF samples are presented in Figs. 3(a) and 3(b), which clearly exhibit PMA and AFM coupling between two CoFeB layers. Here, p-SAF1 is an uncompensated sample [Fig. 3(a)] and p-SAF2 is a nearly compensated sample [Fig. 3(b)] from the remanence at zero field. Both p-SAF samples have strong PMA field $H_k \approx 5$ kOe, and the saturation magnetization of them is about $M_s \approx 1300$ emu/cc. The effective interlayer exchange coupling fields H_{ex} can be evaluated to be ∼200 Oe for p-SAF1 and 100 Oe for p-SAF2. These extracted values can be used as reference parameters for the macrospin simulation. The in-plane hysteresis loops display a hard-axis behavior, and as the in-plane magnetic field increases, the magnetization gradually rotates from the normal direction to in-plane direction of films, but it is hard to see the detailed magnetization process, like the T-type region.

To make clear the magnetization switching in p-SAF samples, we fabricate the Hall bar devices to measure the transport properties. The Hall bar device is shown in the inset of Fig. 3(c). A charge current (I_y) flows through the channel with a width of 20 μm, and meanwhile, the transverse Hall voltage (V_{xy}) is measured. The anomalous Hall resistance ($R_{xy} = V_{xy}/I_y$) is thus obtained. Figures 3(c) and 3(d) show the anomalous Hall resistance as a function of in-plane magnetic field for the p-SAF samples, which are obviously different from the in-plane magnetic hysteresis loops, as shown in Figs. 3(a) and 3(b). In the magnetic hysteresis loops, the normalized magnetization is determined by the projection of the total magnetic moment on the in-plane magnetic field, namely, $M/M_s = (t_1\sin\theta_1 + t_2\sin\theta_2)/(t_1 + t_2)$. This depicts a smooth and monotonically increasing curve, from which it is hard to distinguish the T-type region, while for the R_{xy}-H loops, R_{xy} is dependent on the projection of total magnetization on the Z axis, namely, $R_{xy} \propto (t_1\cos\theta_1 + t_2\cos\theta_2)/(t_1 + t_2)$. This expression is not monotonic. As the magnetic field decreases from +8 kOe to zero, R_{xy} firstly increases from near zero to a large value and then decreases; correspondingly, the magnetization states in p-SAF samples change from the in-plane AFM state to a T-type configuration and then to the perpendicularly magnetized AFM state, as shown in the inset of Fig. 3(d). In other words, with the decrease of the magnetic field, the two perpendicularly magnetized CoFeB layers have different switching response speeds due to their different PMAs. At zero field, R_{xy} of p-SAF1 has a significant value due to the uncompensated magnetization at the normal direction, which is larger than that of the nearly compensated p-SAF2. In addition, the switching fields appear in the R_{xy}-H_y loops but not in the in-plane magnetic hysteresis loops. This is mainly contributed to the magnetization switching in the top CoFeB layer forced by the out-of-plane component of the magnetic field because the in-plane magnetic field is not completely perpendicular to the Néel vector, and moreover, the magnetization in the bottom CoFeB layer also reverses under the

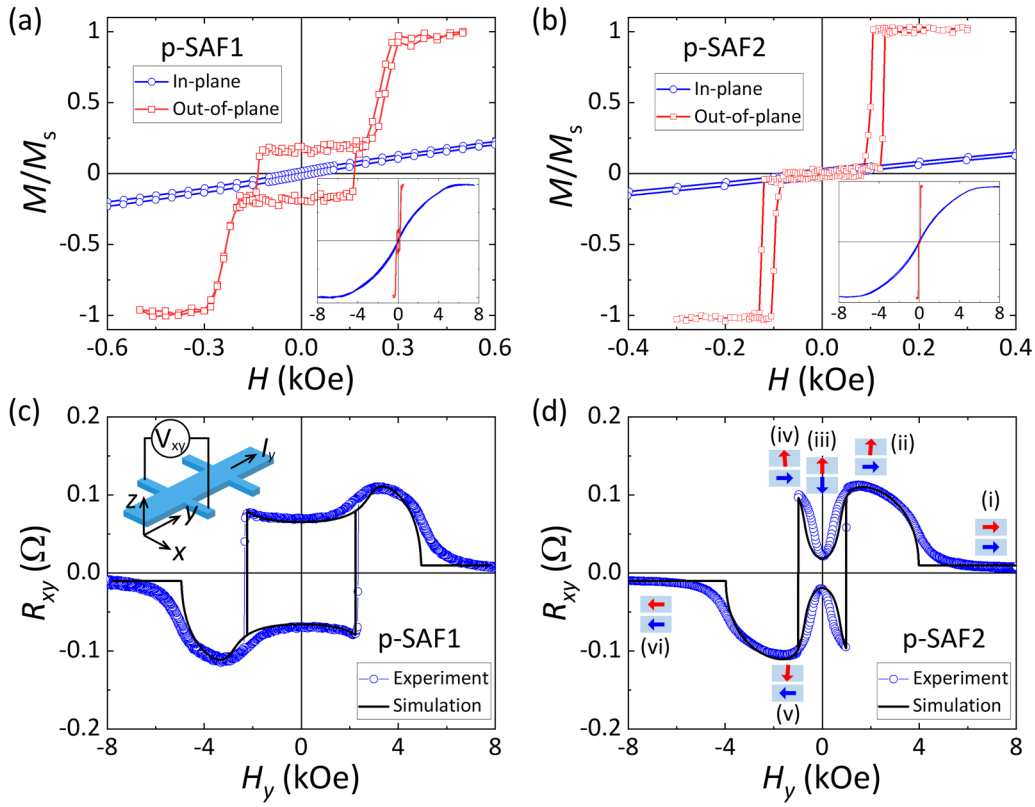

FIG. 3. (a) and (b) Magnetization hysteresis loops of perpendicularly magnetized synthetic antiferromagnet (p-SAF) samples measured under the in-plane and out-of-plane magnetic fields. The insets show the large-scale loops. (c) and (d) Anomalous Hall resistance R_{xy} plotted as a function of in-plane magnetic field H_y measured with a DC current of +2 mA. The black solid lines represent the simulation results. The inset in (c) shows a sketch map of the Hall bar and measurement setup. The insets in (d) show the magnetization state changing from in-plane ferromagnetic (FM) state (i) to T-type state (ii), then to perpendicular antiferromagnetic (AFM) state (iii) at positive magnetic field. When the magnetic field increases inversely, the T-type switches from state (iv) to state (v), and then forms the in-plane FM state (vi).

in-plane magnetic field, as shown by states (iv)–(v) in the inset of Fig. 3(d). Based on the above theoretical model, the equilibrium state of magnetization in a p-SAF can be determined, and we can thus obtain the theoretical results. The experimental R_{xy}-H_y loops are well fitted by numerical simulation results, as shown in Figs. 3(c) and 3(d), in which p-SAF1 and p-SAF2 have the same saturation magnetization $M_s = 1300$ emu/cc, the same interlayer exchange coupling $J_{ex} = 0.02\,\mathrm{erg/cm^2}$, and the same strong PMA field for the top CoFeB layer ($H_{k1} = 4800$ Oe), but they have different PMA fields for the bottom CoFeB layer due to the different thickness ($H_{k2} = 2600$ Oe for p-SAF1 and 1300 Oe for p-SAF2). Obviously, when the in-plane magnetic field H_y is larger than H_{k2} and less than H_{k1}, the magnetization state forms a T-type configuration, in which the magnetization of the bottom CoFeB layer firstly rotates to the in-plane direction (see Appendix A for more detail).

B. Spin wave dispersion

A schematic diagram of the spin wave propagation in the p-SAF sample using BLS measurement is sketched in Fig. 4(a). A laser beam of wavelength $\lambda = 532$ nm shines on the surface of the sample, where the incident angle θ is changed from 10° to 50° and the scattering light is collected from the opposite direction [32–34]. This allows exciting spin waves to have different wave vectors $k = (4\pi/\lambda)\sin\theta$. An external magnetic field is applied along the Y-axis direction, and the wave vector is along the X axis. The BLS spectra are measured at different magnetic fields and wave vectors to obtain the field- and k-dependent variation of resonance frequency. Figures 4(b) and 4(c) display the typical BLS spectra with wave vector $k = 11.8\,\mu\mathrm{m}^{-1}$. Each BLS spectrum includes four peaks, in which the two peaks with negative (positive) frequencies correspond to Stokes (anti-Stokes) modes. Based on the inelastically backscattering geometry, the Stokes and anti-Stokes modes represent the creation and annihilation of a magnon, corresponding to the wave vector along the $+X$ and $-X$ directions, respectively [35,36]. The two Stokes or two anti-Stokes peaks are originated from different resonance modes due to the interlayer exchange coupling in p-SAFs: AM and OM. The low-frequency resonance with higher signal amplitude corresponds to the AM, and the high-frequency resonance with lower signal amplitude corresponds to the OM. When two external magnetic fields with the same strength but opposite directions are applied separately to the p-SAF samples, the resonance frequencies of the AM and OM remain unchanged. This indicates that the spin wave propagation in p-SAFs is reciprocal, which is different from the nonreciprocal propagation in a SAF with easy-plane anisotropy [28,30].

As the magnetic field increases, the resonance frequencies will change, which are plotted in Figs. 5(a) and 5(b). When the external magnetic field is less than the PMA fields of

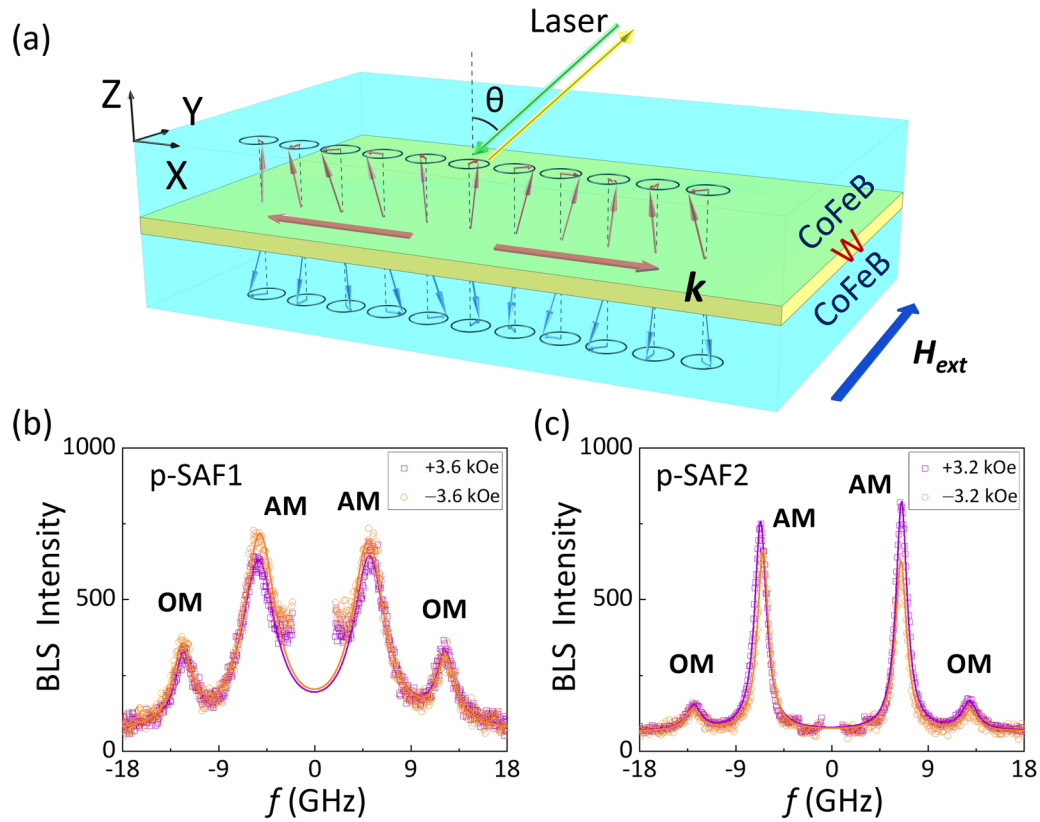

FIG. 4. (a) Schematic of the spin wave propagation in perpendicularly magnetized synthetic antiferromagnet (p-SAF) sample. (b) and (c) Brillouin light scattering (BLS) spectra with wave vector $k = 11.8\,\mu\text{m}^{-1}$ for the p-SAF1 and p-SAF2 samples at different external magnetic fields. The data are fitted through Lorentz peaks, as shown by solid lines.

two CoFeB layers in p-SAFs, namely, $H_{\text{ext}} < H_{k1}$ and H_{k2}, the magnetization is in the AFM state and the BLS spectra present the very weak resonance signal because the probe of BLS in this paper is more sensitive to the in-plane component of magnetization. At a magnetic field with certain strength ($H_{k1} > H_{\text{ext}} > H_{k2}$), the T-type state is established, where the magnetization in the bottom CoFeB layer is aligned to the direction of the magnetic field and the magnetization in the top CoFeB layer mildly deviates from the normal direction. In the T-type region, as the magnetic field increases, the frequency of the OM firstly decreases and then increases, but the frequency of the AM increases. Significantly, there appears a frequency gap due to the coupling between the AM and OM. This gap can be also known as magnon-magnon coupling, which is realized by breaking the rotational symmetry [21,37,38]. At a sufficiently strength magnetic field ($H_{\text{ext}} > H_{k1}$ and H_{k2}),

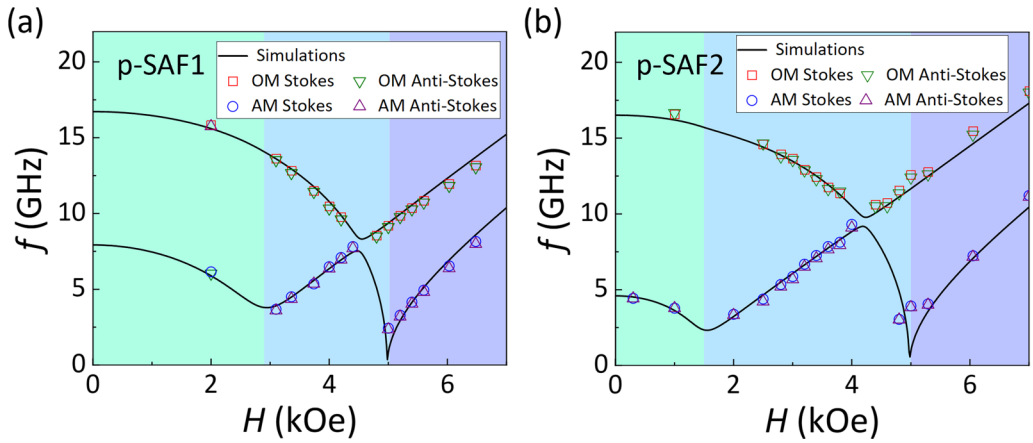

FIG. 5. Dependence of resonance frequencies on external magnetic field for the (a) p-SAF1 and (b) p-SAF2 samples. Experimental data are represented by different symbols, while the black solid lines represent the numerical simulations. The magnetization states are distinguished by using three colored regions. Green, blue, and purple stand for antiferromagnetic (AFM), T-type, and ferromagnetic (FM) states, respectively.

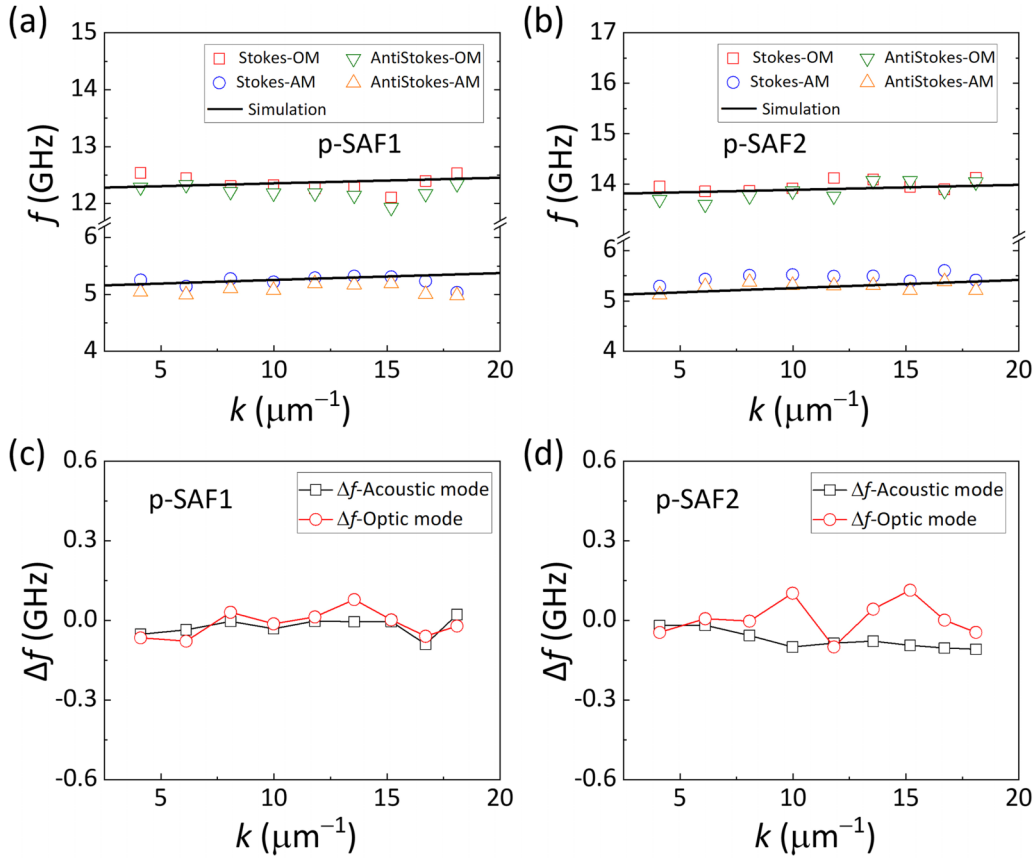

FIG. 6. (a) and (b) The dependence of resonance frequency on wave vector for the p-SAF1 at $H_{ext} = +3.6$ kOe and p-SAF2 at $H_{ext} = +2.8$ kOe. The black solid lines represent the simulation results. (c) and (d) The frequency nonreciprocity Δf as a function of wave vector for the p-SAF1 and p-SAF2 samples.

the FM state is formed and the magnetization in both CoFeB layers is parallel to the direction of the magnetic field. The frequencies of the AM and OM gradually increase with the increase of the magnetic field. Compared with the uncompensated p-SAF1 sample, the nearly compensated p-SAF2 sample has a wider range T-type region and a higher-frequency position of the gap, which are caused by the large difference of PMA fields between top and bottom CoFeB layers. The numerical simulation results are shown by the black solid lines in Figs. 5(a) and 5(b), which are well matched with the experimental data. The simulation parameters are consistent with the above results in R_{xy}-H_y loops for the two p-SAF samples. This demonstrates that the experimental results and theoretical model are self-consistent. The theoretical results also reveal that the stronger interlayer exchange coupling will widen the frequency gap in the T-type region (see Appendix C for more detail). In addition, we also measure the spin wave propagating along the direction of the in-plane magnetic field, namely, the backward volume magnetostatic wave (BVMSW) mode. The results show that the spin wave dispersion of the BVMSW mode is like the case of the wave vector being perpendicular to the magnetic field. The experimental data can also be well fitted by the physical model in this paper (see Appendix D for more detail).

C. Reciprocal spin wave propagation

Figures 6(a) and 6(b) show the dependence of resonance frequencies on the wave vector. Here, the external magnetic fields are set to a certain value to produce the T-type configuration. For both p-SAF samples, the frequencies of the OM and AM are positively related to the wave vector, which are consistent with the simulation results represented by black solid lines. This result indicates that the dynamic dipolar fields would hardly influence the resonance frequency of p-SAF samples in the T-type region. Furthermore, it can be seen microscopically that the frequencies of Stokes modes are slightly larger than that of anti-Stokes modes, which is due to the interfacial DMI in the CoFeB/W/CoFeB multilayers [39,40].

To analyze the nonreciprocity of spin wave propagation, we define the frequency nonreciprocity $\Delta f = [(f^{H+}_{\text{Stokes}} - f^{H-}_{\text{Stokes}}) + (f^{H+}_{\text{anti-S}} - f^{H-}_{\text{anti-S}})]/2$. Note that this expression has excluded the system error from the instrument. Figures 6(c) and 6(d) show the dependence of frequency nonreciprocity Δf on the wave vector for both samples. Here, Δf is within the range of 0.1 GHz for the T-type configuration, then the DMI constant D can be estimated by $\Delta f = \frac{2\gamma}{\pi M_s} Dk$ [41]. When $k = 10\,\mu\text{m}^{-1}$, $D = 0.08\,\text{mJ/m}^2$. This value is slightly less than the reported values ($D = 0.12 - 0.68\,\text{mJ/m}^2$ for W/CoFeB structure) in Refs. [42,43],

which is likely due to the very thin thicknesses of the W and CoFeB layers in this paper. As a result, the small Δf can be ignored due to the weak interfacial DMI. The spin wave propagation in p-SAF samples can be thus considered reciprocal. This reciprocal spin wave has the potential to be applied to wave-based logic circuits, and it can overcome the parasitic scattering in the combiner region of logic elements [44,45].

V. CONCLUSIONS

In summary, we have studied the spin wave dispersion relations in uncompensated and nearly compensated p-SAF samples by using BLS technique, in which an external magnetic field is applied to the perpendicular direction of the Néel vector. The AM and OM are observed in the AFM, T-type, and FM states, and the experimental results can be well explained by the theoretical model. Moreover, we found a frequency gap in the T-type region that is originated from the coupling between the AM and OM. As the wave vector increases, the resonance frequencies increase slightly, and the nonreciprocity $\Delta f < 0.1$ GHz, namely, the spin wave propagation in this case is reciprocal. This paper paves the way for next-generation spin-wave logic devices.

ACKNOWLEDGMENTS

This paper was supported by financial support from the National Key Research and Development Program of China (Grant No. 2021YFB3601300), the National Natural Science Foundation of China (Grants No. 52201290, No. 12074158, No. 12174166, and No. 12104197), and the Fundamental Research Funds for the Central Universities (No. lzujbky-2022-kb01).

APPENDIX A: EQUILIBRIUM STATE OF MAGNETIZATION

The equilibrium state of magnetization in a p-SAF is determined based on the minimum of free energy, namely, $\partial E/\partial\theta_1 = 0$ and $\partial E/\partial\theta_2 = 0$. By solving θ_1 and θ_2 for each magnetic field H_y, the hysteresis loops can be thus obtained by calculating the normalized projection of total magnetization on the Z axis, as shown in Figs. 3(c) and 3(d). In the process of solving the equilibrium equations, the dependence of θ_1 and θ_2 on the magnetic field can be given, as shown in Fig. 7. For both p-SAF samples, the top CoFeB layer has a strong PMA field (H_{k1}), while the bottom CoFeB layer has a weaker PMA field (H_{k2}). Therefore, when the external magnetic field is less than H_{k1} and greater than H_{k2}, the magnetization in the bottom CoFeB layer quickly turns to the in-plane direction, while the magnetization in the top CoFeB layer remains in the out-of-plane direction, forming an approximate upside-down T shape, which can be called the T-type region and marked by the blue area as shown in Fig. 7. Especially for p-SAF2, the H_{k2} of the bottom CoFeB layer is ∼1300 Oe, which is much less than that of the top CoFeB layer. This causes a wide range T-type region, as shown in Fig. 7(b).

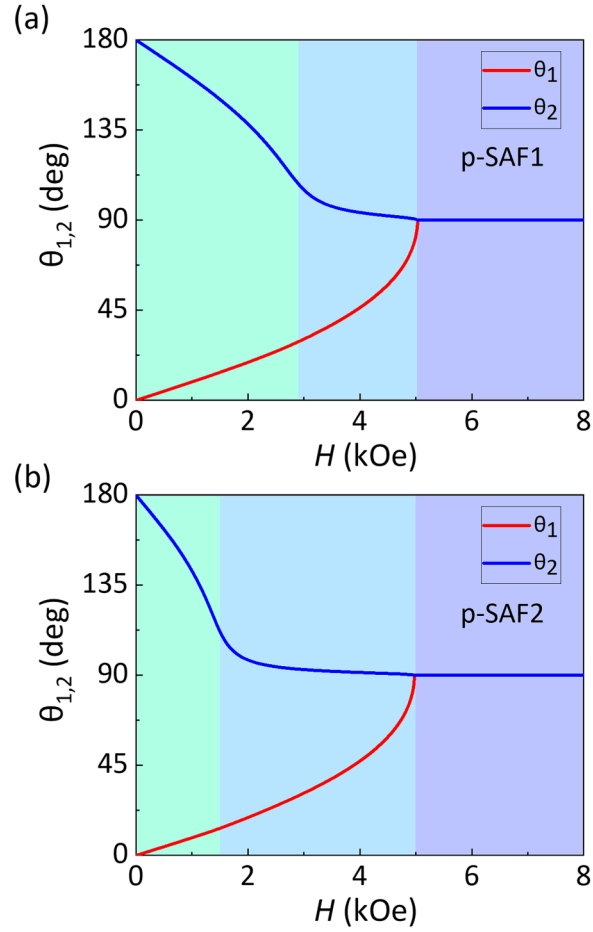

FIG. 7. Dependence of θ_1 and θ_2 on external magnetic field for the (a) p-SAF1 and (b) p-SAF2 samples. Green, blue, and purple areas stand for the antiferromagnetic (AFM), T-type, and ferromagnetic (FM) states, respectively.

APPENDIX B: EFFECTIVE FIELD IN LL EQUATION

On the basis of the total energy density E per unit area of the p-SAF system, the effective field $\vec{H}_i$ acting on the magnetization $\vec{m}_i$ is given by

$$\vec{H}_i = -\nabla_{\vec{m}_i}\left(\frac{E}{\mu_0 M_s t_i}\right) + \vec{h}_{\mathrm{dip},i}, \tag{A1}$$

where $\vec{h}_{\mathrm{dip},i}$ represents the dynamic dipolar field. In the XYZ coordinate, as shown in Fig. 2, the first term of the effective field can be obtained as

$$\vec{H}_1 = \begin{pmatrix} -\frac{H_{ex1}}{M_s} m_{x2} \\ H_{\mathrm{ext}} - H_{ex1}\sin\theta_2 - \frac{H_{ex1}}{M_s}\cos\theta_2 m_{y2} \\ H_{k1}\cos\theta_1 - H_{ex1}\cos\theta_2 - \frac{H_{k1}}{M_s}\sin\theta_1 m_{y1} + \frac{H_{ex1}}{M_s}\sin\theta_2 m_{y2} \end{pmatrix}, \tag{A2}$$

$$\vec{H}_2 = \begin{pmatrix} -\frac{H_{ex2}}{M_s} m_{x1} \\ H_{\mathrm{ext}} - H_{ex2}\sin\theta_1 - \frac{H_{ex2}}{M_s}\cos\theta_1 m_{y1} \\ H_{k2}\cos\theta_2 - H_{ex2}\cos\theta_1 - \frac{H_{k2}}{M_s}\sin\theta_2 m_{y2} + \frac{H_{ex2}}{M_s}\sin\theta_1 m_{y1} \end{pmatrix}. \tag{A3}$$

Here, $H_{ex1} = J_{ex}/(t_1 M_s)$ and $H_{ex2} = J_{ex}/(t_2 M_s)$ are the effective fields of interlayer exchange coupling, $H_{k1} = 2K_1/M_s$ and $H_{k2} = 2K_2/M_s$ are the effective PMA fields, θ_i denotes the angle between the magnetization $\vec{m}_i$ and the Z axis. Note that the DMI field only leads to a shift of the dispersion relation, depending on the wave vector. Therefore, the final dispersion relation can be expressed as $f_0(k, H) + \Delta f$, and $\Delta f = \frac{2\gamma}{\pi M_s} Dk$ [41]. Here, D is the interfacial DMI constant.

By assuming $kt \ll 1$ and considering Maxwell's relations $\nabla \cdot \vec{B} = 0$ and $\nabla \times \vec{h}_{\mathrm{dip},i} = 0$, the dynamic dipolar field $\vec{h}_{\mathrm{dip},i}$ can be given by [46,47]

$$\vec{h}_{\mathrm{dip},1} = -2\pi k t_1 \begin{pmatrix} m_{x1} \\ 0 \\ 0 \end{pmatrix} - 2\pi k t_2 \begin{pmatrix} m_{x2} \\ 0 \\ i m_{x2} \end{pmatrix}, \tag{A4}$$

$$\vec{h}_{\mathrm{dip},2} = -2\pi k t_2 \begin{pmatrix} m_{x2} \\ 0 \\ 0 \end{pmatrix} - 2\pi k t_1 \begin{pmatrix} m_{x1} \\ 0 \\ i m_{x1} \end{pmatrix}, \tag{A5}$$

where the first term is the self-dipolar field and the second term is the mutual-dipolar field. To simplify two sets of coupled LL equations in p-SAFs, a new xyz coordinate is established, as shown in Fig. 2. The effective fields can be transformed from the XYZ coordinate to the xyz coordinate by using a rotation matrix, which is given by

$$A = \begin{pmatrix} 1 & 0 & 0 \\ 0 & \cos\theta_i & -\sin\theta_i \\ 0 & \sin\theta_i & \cos\theta_i \end{pmatrix}. \tag{A6}$$

In the xyz coordinate, the effective field can be expressed as $\vec{H}_{\mathrm{eff},i} = A\vec{H}_i$, and the LL in Eq. (A1) can be thus linearized as

$$\begin{pmatrix} i\omega/\gamma & A_{12} & A_{13} & A_{14} \\ A_{21} & i\omega/\gamma & A_{23} & A_{24} \\ A_{31} & A_{32} & i\omega/\gamma & A_{34} \\ A_{41} & A_{42} & A_{43} & i\omega/\gamma \end{pmatrix} \begin{pmatrix} m_{x1} \\ m_{y1} \\ m_{x2} \\ m_{y2} \end{pmatrix} = 0, \tag{A7}$$

where the matrix elements are given by

$$\begin{aligned}
A_{12} &= H_{\mathrm{ext}}\sin\theta_1 + H_{k1}\cos^2\theta_1 - H_{\mathrm{ex1}}\cos(\theta_1 - \theta_2) \\
&\quad - H_{k1}\sin^2\theta_1, \\
A_{13} &= -2\pi M_s i k t_2 \sin\theta_1, \\
A_{14} &= H_{\mathrm{ex1}}\cos(\theta_1 - \theta_2), \\
A_{21} &= -H_{\mathrm{ext}}\sin\theta_1 - H_{k1}\cos^2\theta_1 + H_{\mathrm{ex1}}\cos(\theta_1 - \theta_2) \\
&\quad - 2\pi M_s k t_1, \\
A_{23} &= -H_{\mathrm{ex1}} - 2\pi M_s k t_2, \\
A_{24} &= A_{42} = 0, \\
A_{31} &= -2\pi M_s i k t_1 \sin\theta_2, \\
A_{32} &= H_{\mathrm{ex2}}\cos(\theta_1 - \theta_2), \\
A_{34} &= H_{\mathrm{ext}}\sin\theta_2 + H_{k2}\cos^2\theta_2 - H_{\mathrm{ex2}}\cos(\theta_1 - \theta_2) \\
&\quad - H_{k2}\sin^2\theta_2, \\
A_{41} &= -H_{\mathrm{ex2}} - 2\pi M_s k t_1, \\
A_{43} &= -H_{\mathrm{ext}}\sin\theta_2 - H_{k2}\cos^2\theta_2 + H_{\mathrm{ex2}}\cos(\theta_1 - \theta_2) \\
&\quad - 2\pi M_s k t_2.
\end{aligned}$$

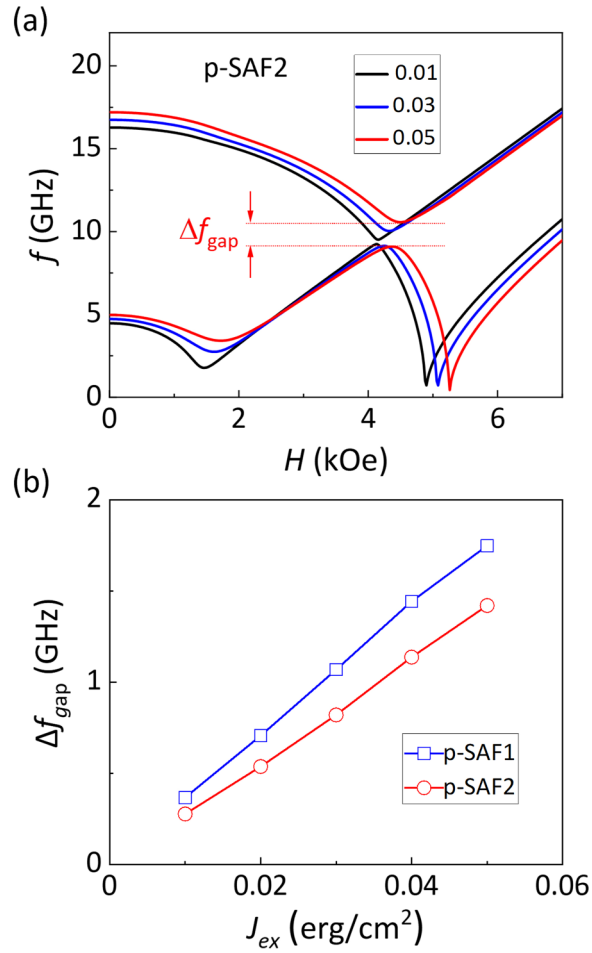

FIG. 8. Simulation results of magnon-magnon coupling. (a) Dependence of resonance frequencies on magnetic field for p-SAF2 with different interlayer exchange energy J_{ex}. (b) The frequency gap as a function of J_{ex} for p-SAF1 and p-SAF2.

To solve Eq. (A7), the determinant of the coefficient matrix must be equal to zero. Therefore, we can obtain the dependence of resonance frequency on the magnetic field and the wave vector by numerical calculation.

APPENDIX C: MAGNON-MAGNON COUPLING IN T-TYPE REGION

Figure 8 shows the simulation results of magnon-magnon coupling in the T-type region with different interlayer exchange energy J_{ex}. As J_{ex} increases for the p-SAF2 sample, as shown in Fig. 8(a), the frequency gap gradually widens, and the position of resonance fields moves to the high field. When the interlayer exchange energy $J_{ex} = 0.05\,\mathrm{erg/cm^2}$, the frequency gap reaches 1.42 GHz. Figure 8(b) shows the dependence of the frequency gap on J_{ex}. The frequency gap increases linearly with the increase of interlayer exchange energy J_{ex}. Moreover, compared with the p-SAF2 sample, p-SAF1 has larger frequency gaps due to its strong PMA field of the bottom CoFeB layer. This result is vital for the quantum magnonics, and it needs to be studied through more experimental results.

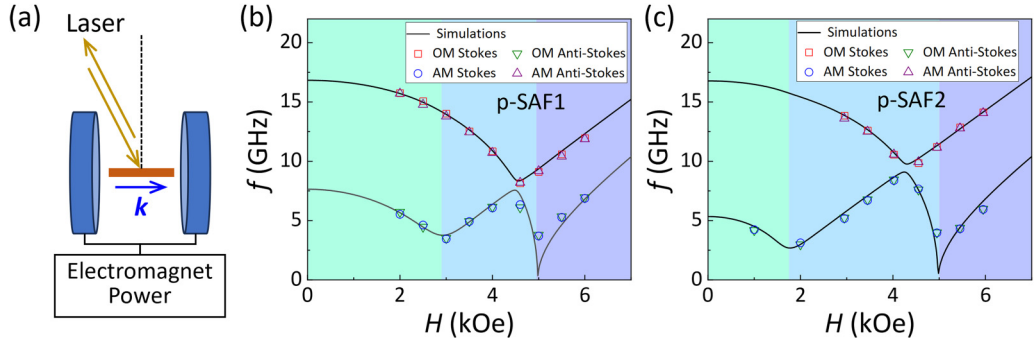

FIG. 9. (a) Sketch map of the configuration of spin wave propagation and external magnetic field. (b) and (c) Dependence of resonance frequencies on external magnetic field for the p-SAF1 and p-SAF2 samples.

APPENDIX D: BVMSW

Figure 9(a) shows the sketch map of the BLS measurement, in which the spin wave propagates along the direction of the external magnetic field. Due to the influence of the electromagnet on the optical path, BLS spectra are only measured at the incident angle $\theta = 20^\circ$ ($k = 8.1\,\mu\text{m}^{-1}$). In this configuration, the excited spin wave is a BVMSW mode [1]. Figures 9(b) and 9(c) show the dependence of resonance frequencies on the external magnetic field for the p-SAF1 and p-SAF2 samples. We also fit the experimental data by the physical model in this paper, as shown by the black solid lines. For the two cases of $k \,//\, H$ and $k \perp H$, only the dynamical dipolar fields are different, and the total energy of the SAF system is the same. Therefore, their dependences of frequency on the magnetic field are almost identical.

[1] A. A. Serga, A. V. Chumak, and B. Hillebrands, YIG magnonics, J. Phys. D: Appl. Phys. **43**, 264002 (2010).

[2] A. V. Chumak, V. I. Vasyuchka, A. A. Serga, and B. Hillebrands, Magnon spintronics, Nat. Phys. **11**, 453 (2015).

[3] A. Barman, G. Gubbiotti, S. Ladak, A. O. Adeyeye, M. Krawczyk, J. Gräfe, C. Adelmann, S. Cotofana, A. Naeemi, V. I. Vasyuchka *et al.*, The 2021 magnonics roadmap, J. Phys.: Condens. Matter **33**, 413001 (2021).

[4] Q. Wang, A. V. Chumak, and P. Pirro, Inverse-design magnonic devices, Nat. Commun. **12**, 2636 (2021).

[5] A. V. Chumak, P. Kabos, M. Wu, C. Abert, C. Adelmann, A. O. Adeyeye, J. Åkerman, F. G. Aliev, A. Anane, A. Awad *et al.*, Advances in magnetics roadmap on spin-wave computing, IEEE Trans. Magn. **58**, 1 (2022).

[6] A. V. Chumak, A. A. Serga, and B. Hillebrands, Magnon transistor for all-magnon data processing, Nat. Commun. **5**, 4700 (2014).

[7] Á. Papp, W. Porod, and G. Csaba, Nanoscale neural network using non-linear spin-wave interference, Nat. Commun. **12**, 6422 (2021).

[8] A. Khitun, M. Bao, and K. L. Wang, Magnonic logic circuits, J. Phys. D: Appl. Phys. **43**, 264005 (2010).

[9] J. Chen, F. Heimbach, T. Liu, H. Yu, C. Liu, H. Chang, T. Stückler, J. Hu, L. Zeng, Y. Zhang *et al.*, Spin wave propagation in perpendicularly magnetized nm-thick yttrium iron garnet films, J. Magn. Magn. Mater. **450**, 3 (2018).

[10] M. S. Alam, C. Wang, J. Chen, J. Zhang, C. Liu, J. Xiao, Y. Wu, L. Bi, and H. Yu, Temperature control of spin wave propagation over 100 μm distance in 100 nm-thick YIG film, Phys. Lett. A **383**, 366 (2019).

[11] J. Chen, T. Yu, C. Liu, T. Liu, M. Madami, K. Shen, J. Zhang, S. Tu, M. S. Alam, K. Xia *et al.*, Excitation of unidirectional exchange spin waves by a nanoscale magnetic grating, Phys. Rev. B **100**, 104427 (2019).

[12] B. Divinskiy, H. Merbouche, K. O. Nikolaev, S. M. de Vasconcellos, R. Bratschitsch, D. Gouéré, R. Lebrun, V. Cros, J. Ben Youssef, P. Bortolotti *et al.*, Dispersionless propagation of ultrashort spin-wave pulses in ultrathin yttrium iron garnet waveguides, Phys. Rev. Appl. **16**, 024028 (2021).

[13] Z. Duan, C. T. Boone, X. Cheng, I. N. Krivorotov, N. Reckers, S. Stienen, M. Farle, and J. Lindner, Spin-wave modes in permalloy/platinum wires and tuning of the mode damping by spin Hall current, Phys. Rev. B **90**, 024427 (2014).

[14] P. Malagò, L. Giovannini, R. Zivieri, P. Gruszecki, and M. Krawczyk, Spin-wave dynamics in permalloy/cobalt magnonic crystals in the presence of a nonmagnetic spacer, Phys. Rev. B **92**, 064416 (2015).

[15] M. Nakayama, K. Yamanoi, S. Kasai, S. Mitani, and T. Manago, Thickness dependence of spin wave nonreciprocity in permalloy film, Jpn. J. Appl. Phys. **54**, 083002 (2015).

[16] V. Baltz, A. Manchon, M. Tsoi, T. Moriyama, T. Ono, and Y. Tserkovnyak, Antiferromagnetic spintronics, Rev. Mod. Phys. **90**, 015005 (2018).

[17] P. Vaidya, S. A. Morley, J. van Tol, Y. Liu, R. Cheng, A. Brataas, D. Lederman, and E. del Barco, Subterahertz spin pumping from an insulating antiferromagnet, Science **368**, 160 (2020).

[18] A. Legros, S. S. Zhang, X. Bai, H. Zhang, Z. Dun, W. A. Phelan, C. D. Batista, M. Mourigal, and N. P. Armitage, Observation of 4- and 6-magnon bound states in the spin-anisotropic frustrated antiferromagnet FeI_2, Phys. Rev. Lett. **127**, 267201 (2021).

[19] J. Han, P. Zhang, Z. Bi, Y. Fan, T. S. Safi, J. Xiang, J. Finley, L. Fu, R. Cheng, and L. Liu, Birefringence-like spin transport via linearly polarized antiferromagnetic magnons, Nat. Nanotechnol. **15**, 563 (2020).

[20] M. Hamdi, F. Posva, and D. Grundler, Spin wave dispersion of ultra-low damping hematite (α-Fe_2O_3) at GHz frequencies, Phys. Rev. Mater. **7**, 054407 (2023).

[21] D. MacNeill, J. T. Hou, D. R. Klein, P. Zhang, P. Jarillo-Herrero, and L. Liu, Gigahertz frequency antiferromagnetic resonance and strong magnon-magnon coupling in the layered crystal $CrCl_3$, Phys. Rev. Lett. **123**, 047204 (2019).

[22] R. Cheng, M. W. Daniels, J.-G. Zhu, and D. Xiao, Antiferromagnetic spin wave field-effect transistor, Sci. Rep. **6**, 24223 (2016).

[23] J. Walowski and M. Münzenberg, Perspective: Ultrafast magnetism and THz spintronics, J. Appl. Phys. **120**, 140901 (2016).

[24] J. R. Hortensius, D. Afanasiev, M. Matthiesen, R. Leenders, R. Citro, A. V. Kimel, R. V. Mikhaylovskiy, B. A. Ivanov, and A. D. Caviglia, Coherent spin-wave transport in an antiferromagnet, Nat. Phys. **17**, 1001 (2021).

[25] Y. Shiota, T. Taniguchi, M. Ishibashi, T. Moriyama, and T. Ono, Tunable magnon-magnon coupling mediated by dynamic dipolar interaction in synthetic antiferromagnets, Phys. Rev. Lett. **125**, 017203 (2020).

[26] A. Sud, Y. Koike, S. Iihama, C. Zollitsch, S. Mizukami, and H. Kurebayashi, Parity-controlled spin-wave excitations in synthetic antiferromagnets, Appl. Phys. Lett. **118**, 032403 (2021).

[27] R. A. Gallardo, T. Schneider, A. K. Chaurasiya, A. Oelschlägel, S. S. P. K. Arekapudi, A. Roldán-Molina, R. Hübner, K. Lenz, A. Barman, J. Fassbender *et al.*, Reconfigurable spin-wave nonreciprocity induced by dipolar interaction in a coupled ferromagnetic bilayer, Phys. Rev. Appl. **12**, 034012 (2019).

[28] M. Ishibashi, Y. Shiota, T. Li, S. Funada, T. Moriyama, and T. Ono, Switchable giant nonreciprocal frequency shift of propagating spin waves in synthetic antiferromagnets, Sci. Adv. **6**, eaaz6931 (2020).

[29] M. Ishibashi, Y. Shiota, S. Funada, T. Moriyama, and T. Ono, Spin wave resonance in perpendicularly magnetized synthetic antiferromagnets, J. Magn. Soc. Jpn. **45**, 25 (2021).

[30] O. Gladii, R. Salikhov, O. Hellwig, H. Schultheiss, J. Lindner, and R. A. Gallardo, Spin-wave nonreciprocity at the spin-flop transition region in synthetic antiferromagnets, Phys. Rev. B **107**, 104419 (2023).

[31] T. Chiba, G. E. W. Bauer, and S. Takahashi, Magnetization damping in noncollinear spin valves with antiferromagnetic interlayer couplings, Phys. Rev. B **92**, 054407 (2015).

[32] W. Song, X. Wang, C. Jia, X. Wang, C. Jiang, D. Xue, and G. Chai, Nonreciprocal emergence of hybridized magnons in magnetic thin films, Phys. Rev. B **104**, 014402 (2021).

[33] C. W. Sandweg, M. B. Jungfleisch, V. I. Vasyuchka, A. A. Serga, P. Clausen, H. Schultheiss, B. Hillebrands, A. Kreisel, and P. Kopietz, Wide-range wavevector selectivity of magnon gases in Brillouin light scattering spectroscopy, Rev. Sci. Instrum. **81**, 073902 (2010).

[34] W. Song, X. Wang, W. Wang, C. Jiang, X. Wang, and G. Chai, Backward magnetostatic surface spin waves in coupled Co/FeNi bilayers, Phys. Status. Solidi RRL **14**, 2000118 (2020).

[35] S. O. Demokritov, B. Hillebrands, and A. N. Slavin, Brillouin light scattering studies of confined spin waves: Linear and nonlinear confinement, Phys. Rep. **348**, 441 (2001).

[36] F. Kargar and A. A. Balandin, Advances in Brillouin-Mandelstam light-scattering spectroscopy, Nat. Photon. **15**, 720 (2021).

[37] M. Li, J. Lu, and W. He, Symmetry breaking induced magnon-magnon coupling in synthetic antiferromagnets, Phys. Rev. B **103**, 064429 (2021).

[38] C. Dai and F. Ma, Strong magnon-magnon coupling in synthetic antiferromagnets, Appl. Phys. Lett. **118**, 112405 (2021).

[39] T. Brächer, O. Boulle, G. Gaudin, and P. Pirro, Creation of unidirectional spin-wave emitters by utilizing interfacial Dzyaloshinskii-Moriya interaction, Phys. Rev. B **95**, 064429 (2017).

[40] D. Cortés-Ortuño and P. Landeros, Influence of the Dzyaloshinskii-Moriya interaction on the spin-wave spectra of thin films, J. Phys.: Condens. Matter **25**, 156001 (2013).

[41] A. K. Chaurasiya, S. Choudhury, J. Sinha, and A. Barman, Dependence of interfacial Dzyaloshinskii-Moriya interaction on layer thicknesses in Ta/Co-Fe-B/TaO_x heterostructures from Brillouin light scattering, Phys. Rev. Appl. **9**, 014008 (2018).

[42] R. Soucaille, M. Belmeguenai, J. Torrejon, J.-V. Kim, T. Devolder, Y. Roussigné, S.-M. Chérif, A. A. Stashkevich, M. Hayashi, and J.-P. Adam, Probing the Dzyaloshinskii-Moriya interaction in CoFeB ultrathin films using domain wall creep and Brillouin light spectroscopy, Phys. Rev. B **94**, 104431 (2016).

[43] S. Jaiswal, K. Litzius, I. Lemesh, F. Büttner, S. Finizio, J. Raabe, M. Weigand, K. Lee, J. Langer, B. Ocker *et al.*, Investigation of the Dzyaloshinskii-Moriya interaction and room temperature skyrmions in W/CoFeB/MgO thin films and microwires, Appl. Phys. Lett. **111**, 022409 (2017).

[44] S. Klingler, P. Pirro, T. Brächer, B. Leven, B. Hillebrands, and A. V. Chumak, Design of a spin-wave majority gate employing mode selection, Appl. Phys. Lett. **105**, 152410 (2014).

[45] S. Klingler, P. Pirro, T. Brächer, B. Leven, B. Hillebrands, and A. V. Chumak, Spin-wave logic devices based on isotropic forward volume magnetostatic waves, Appl. Phys. Lett. **106**, 212406 (2015).

[46] R. L. Stamps, Spin configurations and spin-wave excitations in exchange-coupled bilayers, Phys. Rev. B **49**, 339 (1994).

[47] I. A. Armijo and R. E. Arias, Spin wave modes of multilayered ferromagnetic films, Phys. Rev. B **99**, 014432 (2019).